nature materials

Article

https://doi.org/10.1038/s41563-024-02096-4

Printable molecule-selective core–shell nanoparticles for wearable and implantable sensing

Received: 31 December 2023

Accepted: 2 December 2024

Published online: 03 February 2025

Check for updates

Minqiang Wang[1,6], Cui Ye[1,6], Yiran Yang[1], Daniel Mukasa[2], Canran Wang[1], Changhao Xu[1], Jihong Min[1], Samuel A. Solomon[1], Jiaobing Tu[1], Guofang Shen[3], Songsong Tang[1], Tzung K. Hsiai[4], Zhaoping Li[5], Jeannine S. McCune[3] & Wei Gao[1]

Wearable and implantable biosensors are pioneering new frontiers in precision medicine by enabling continuous biomolecule analysis for fundamental investigation and personalized health monitoring. However, their widespread adoption remains impeded by challenges such as the limited number of detectable targets, operational instability and production scalability. Here, to address these issues, we introduce printable core–shell nanoparticles with built-in dual functionality: a molecularly imprinted polymer shell for customizable target recognition, and a nickel hexacyanoferrate core for stable electrochemical transduction. Using inkjet printing with an optimized nanoparticle ink formulation, we demonstrate the mass production of robust and flexible biosensors capable of continuously monitoring a broad spectrum of biomarkers, including amino acids, vitamins, metabolites and drugs. We demonstrate their effectiveness in wearable metabolic monitoring of vitamin C, tryptophan and creatinine in individuals with long COVID. Additionally, we validate their utility in therapeutic drug monitoring for cancer patients and in a mouse model through providing real-time analysis of immunosuppressants such as busulfan, cyclophosphamide and mycophenolic acid.

Monitoring the dynamic profiles of circulating molecules—encompassing nutrients, metabolites, hormones and medications—at a personalized level is essential for gaining insights into an individual's physiological health[1–4]. Unlike traditional laboratory-based blood analyses, which are time-intensive and produce delayed, discrete data points, wearable and implantable biosensors offer an attractive solution. These devices enable wireless, high-temporal-resolution capture of real-time molecular fluctuations[5–10], facilitating early detection of abnormal health conditions and timely interventions, while also advancing the discovery of next-generation biomarkers for precision medicine[11–14].

Despite their potential, wearable and implantable biosensors face substantial challenges. Currently, only a small number of analytes can be continuously monitored in real-time and at the point of need[8,15]. Additionally, many existing wearable biosensors struggle with limited operational longevity in biofluids, often due to the instability

[1]Andrew and Peggy Cherng Department of Medical Engineering, Division of Engineering and Applied Science, California Institute of Technology, Pasadena, CA, USA. [2]Department of Applied Physics and Materials Science, Division of Engineering and Applied Science, California Institute of Technology, Pasadena, CA, USA. [3]Department of Hematologic Malignancy Translational Sciences, Beckman Research Institute at City of Hope, Duarte, CA, USA. [4]Division of Cardiology, David Geffen School of Medicine, University of California, Los Angeles, Los Angeles, CA, USA. [5]Division of Clinical Nutrition, David Geffen School of Medicine, University of California, Los Angeles, Los Angeles, CA, USA. [6]These authors contributed equally: Minqiang Wang, Cui Ye.
e-mail: weigao@caltech.edu

https://doi.org/10.1038/s41563-024-02096-4

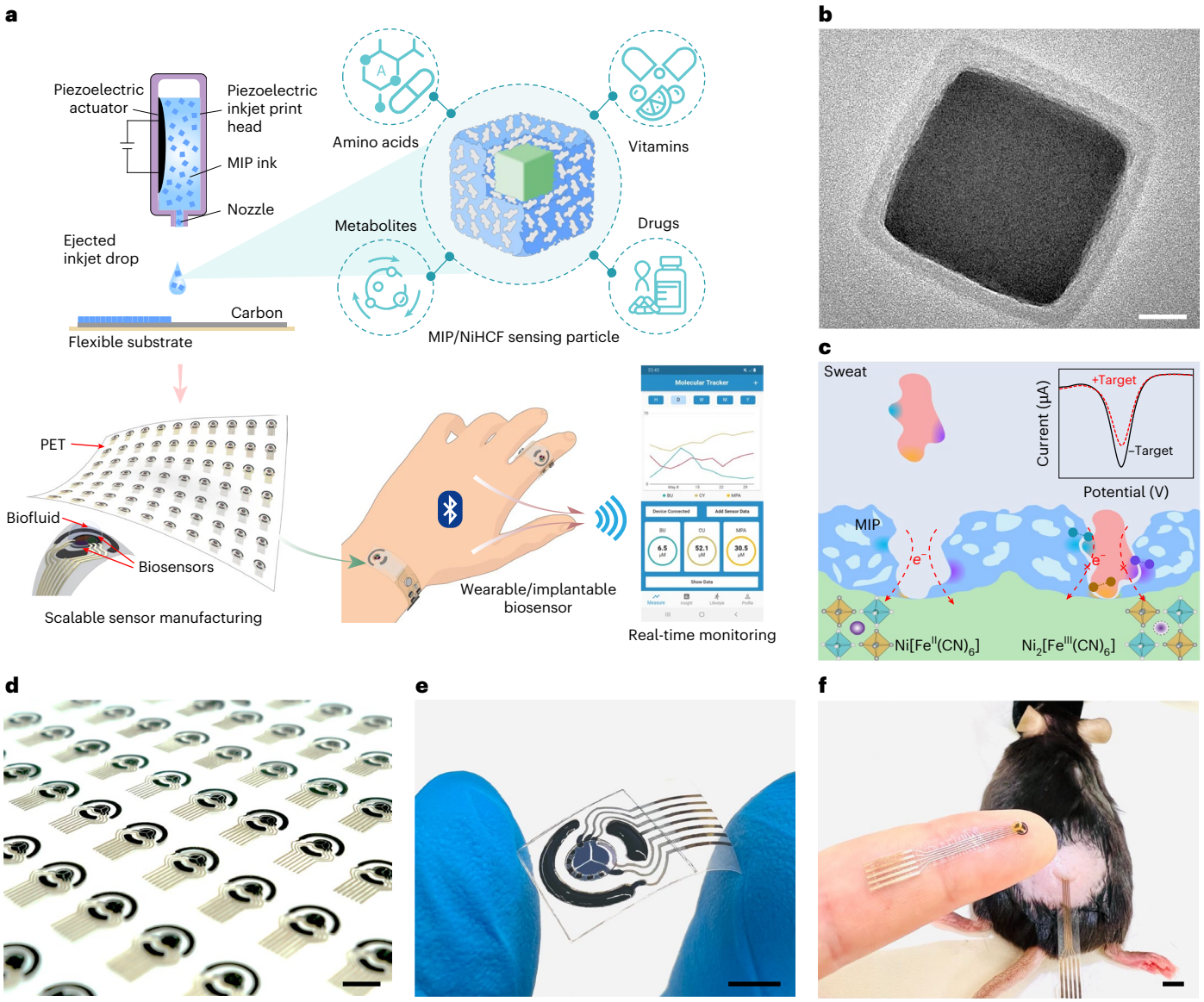

Fig. 1 | Printable molecule-selective core–shell nanoparticles for wearable and implantable biosensing. a, Schematic of inkjet-printable core–shell cubic nanoparticles with the dual capability of molecule recognition and signal transduction for mass production of highly stable wearable and implantable sensors capable of real-time monitoring of various circulating biomarkers such as amino acids, vitamins, metabolites and drugs. **b**, TEM image of a core–shell nanoparticle consisting of an MIP shell and a redox-active core based on a PBA NiHCF. Scale bar, 25 nm. **c**, Electrochemical sensing mechanism of the MIP/NiHCF nanoparticle: the MIP shell selectively recognizes the target molecules and alters the redox signal of the NiHCF core. **d**, Optical image of flexible sensor arrays mass-produced via inkjet printing of MIP/NiHCF nanoparticles. Scale bar, 5 mm. **e**,**f**, Photographs of a wearable patch for non-invasive multiplexed sweat biomarker analysis (**e**) and sensor patches implanted subcutaneously in a mouse for real-time interstitial fluid biomarker analysis (**f**). Scale bars, 5 mm.

of redox probes or bioreceptors[16–19]. Furthermore, despite advances in scalable electrode fabrication technologies[20,21], labour-intensive bioreceptor modification steps still hinder the reproducibility of sensor performance.

To address these challenges and meet the growing need for personalized health monitoring, we present solution-synthesized core–shell nanoparticles with built-in dual-functional capabilities, offering tunable target molecule recognition and stable electrochemical signal transduction. These nanoparticles enable scalable manufacturing of robust wearable and implantable biosensors capable of selectively and continuously monitoring a broad spectrum of circulating biomarkers including amino acids, vitamins, metabolites and drugs (Fig. 1a). The core–shell nanoparticle comprises a molecularly imprinted polymer (MIP) shell for selective binding[22,23] and a Prussian blue analogue (PBA)-based redox-active core to generate measurable electrochemical signals[24] (Fig. 1b). As the target molecules adsorb onto the binding sites located on the MIP shell, electron transfer between the PBA core and the biofluid is impeded, reducing the redox signal, which is quantified by differential pulse voltammetry (DPV) (Fig. 1c). The use of a nickel hexacyanoferrate (NiHCF) core imparts high redox-reaction stability in biological fluids, ideal for long-term applications of wearable and implantable sensors. The flexible sensor arrays can be fabricated at scale and low cost through inkjet printing of optimized core–shell nanoparticle inks (Fig. 1d). Compared to prior biosensors, these printed biosensors offer several advantages, namely, scalable manufacturing with minimal manual handling, versatility in targeting various analytes, cost-effectiveness, and long-term stability for both storage and body fluid analysis. Importantly, the streamlined printing process eliminates manual sensor modification, resulting in consistent, mass-producible biosensors with minimal sensor-to-sensor variations.

By addressing critical challenges in wearable and implantable biosensors through functional materials, this technology extends to a wide range of personalized health applications. For instance, we demonstrate the use of printed biosensors for non-invasive wearable biomarker sensing through automatic and multiplexed sweat analysis (Fig. 1e). Additionally, they can be subcutaneously implanted for real-time biomarker analysis within interstitial fluid (Fig. 1f). Using vitamin C, also known as ascorbic acid (AA), tryptophan (Trp) and creatinine (CK) as model analytes, we showcase the potential of these nanoparticles in wearable biosensors for long COVID investigations in human trials involving healthy participants and individuals with long COVID. We also validated the sensors for therapeutic drug monitoring (TDM) in cancer patients and in a mouse model through real-time analysis of immunosuppressants such as busulfan (BU), cyclophosphamide (CY) and mycophenolic acid (MPA).

Fabrication and optimization of core–shell nanoparticles for high-performance biosensing

A solution-based synthetic method incorporating citrate as a chelating agent was used to regulate the reaction rate in the synthesis of PBAs[25]. This led to the scalable production of highly uniform PBA nanocubes, which served as the core for subsequent core–shell nanoparticle preparation (Fig. 2a,b). It should be noted that although alternative redox probes such as methylene blue or ferrocene could be valuable for various biosensing applications, their high water solubility poses a substantial challenge when preparing inkjet-printable nanoparticles. We successfully synthesized PBA nanocubes with various transition metals (that is, iron, cobalt, nickel and copper) that exhibited strong redox activities under a suitable applied potential. Dark-field scanning transmission electron microscopy (DF-STEM) and energy-dispersive X-ray spectroscopy (EDS) analyses of these nanocubes confirmed a uniform length size of approximately 100 nm and an even distribution of the metal ions (Fig. 2c).

In long-term wearable and implantable sensing applications, the electrochemical stability of PBA nanocubes is crucial[26]. Despite the widespread use of Prussian blue (FeHCF) as an electron-transfer mediator in electrochemical sensors[18,27], it exhibits poor stability during extended testing in physiologically relevant fluids such as phosphate-buffered saline (PBS). Reduced redox signals and structural degradation of the FeHCF cubes occurred after 50 repetitive cyclic voltammetry (CV) scans (Fig. 2d). The PBA nanocubes showed varying levels of stability, with an order of NiHCF > CoHCF > CuHCF > FeHCF (Fig. 2e and Supplementary Fig. 1). X-ray diffraction analysis further confirmed that NiHCF retained its cubic structure with minimal degradation even after 5,000 cycles of CV scans, while CoHCF and CuHCF experienced substantial crystallographic integrity loss (Fig. 2f and Supplementary Fig. 2). Such high stability can be attributed to the enhanced lattice stability during ion (for example, Na^+, K^+) insertion/extraction processes, arising from zero-strain characteristics resulting from the substitution of iron in PB with small-radius metal atoms (such as nickel)[28–30] (Fig. 2g and Supplementary Fig. 3).

To prepare the dual-function core–shell sensing nanoparticles, a solution comprising suitable monomer, cross-linker and target molecules undergoes preadsorption and thermal polymerization, forming a thin MIP layer on the surface of the NiHCF nanocubes (Fig. 2h). Subsequent extraction of target molecules yields target-selective cavities within the MIP shell, exposing the NiHCF core to the sample matrix. The resulting MIP/NiHCF core–shell nanoparticles are able to selectively recognize target molecules, with increased cavity–molecule bonding leading to reduced exposure of NiHCF that is quantifiable through DPV (Fig. 2h).

STEM and EDS characterizations of the MIP/NiHCF nanoparticles reveal homogeneous distributions of elemental nickel and iron within the cubic core, along with oxygen in the polymeric structure originating from the MIP across the nanoparticle surface (Fig. 2i). These findings underscore the successful core–shell nanoparticle synthesis. Additionally, Fourier-transform infrared spectroscopy (FTIR) was used to characterize the synthesis of a target-selective MIP shell with the immunosuppressive drug CY as the target molecule. The emergence and subsequent disappearance of a characteristic peak (that is, the C–Cl bond from CY[31]) at approximately 657 cm^{-1} upon MIP introduction and target extraction, respectively, confirm the successful fabrication of the CY MIP shell (Fig. 2j).

Given the complexity of MIP optimization, QuantumDock, an automated computational framework[32], was used to identify the most suitable monomer choice for preparing MIP shells with desired sensitivity and selectivity towards in situ wearable and implantable biomarker analysis. Using AA as an exemplar target molecule, QuantumDock identified stable binding sites and geometries via molecular docking (Fig. 2k) and assessed the binding energies and differences between monomer/target and monomer/interferent molecules via density functional theory (DFT) (Fig. 2l and Supplementary Fig. 4). Methacrylic acid (MAA) emerged as the optimal monomer for AA analysis due to high average sensitivity and selectivity against interferents with chemical structures similar to AA. The monomer choice was further validated experimentally through ultraviolet–visible spectrophotometry, in which MAA-based MIP/NiHCF nanoparticles demonstrated the highest target absorption (Fig. 2m and Supplementary Fig. 5).

For in vivo target biomarker monitoring applications, it is imperative to confirm the cytocompatibility of the MIP/NiHCF nanoparticles. To assess the impact on cell viability, cells were cultured in media containing 5 and 20 μg ml^{-1} nanoparticles, and their viability was examined using a commercially available live/dead assay kit. Live/dead staining images of human dermal fibroblasts (HDFs) over extended culture periods (Fig. 2n,o) demonstrated robust cell viability, underscoring the high cytocompatibility of MIP/NiHCF nanoparticles. This observation supports the potential utility of these nanoparticles for in vivo biomarker monitoring without compromising cellular health.

Scalable printing of core–shell nanoparticle-based high-performance biosensors

Droplet inkjet printing is a highly promising approach for scalable and cost-effective manufacturing of physiochemical biosensors[20]. Customized MIP/NiHCF nanoparticle inks are tailored to meet the viscosity, density and surface tension required for inkjet printing (Fig. 3a). A systematic approach, involving computationally assisted optimization of various solvents alongside experimental validation, was used to pinpoint a solvent that could achieve the desired viscosity and uniform dispersion of the MIP/NiHCF nanoparticle ink (Fig. 3b and Supplementary Figs. 6 and 7). Dipole moments of solvents were calculated as a measure of their polarity, which we visualize via the highest occupied molecular orbital (HOMO). Solvents with higher moments are more likely to form strong dipole–dipole interactions with MIP/NiHCF nanoparticles, shielding them from self-interaction and subsequent aggregation. Following this logic, we identified an optimal solvent blend consisting of ethanol, water and *N*-methylpyrrolidone (NMP) in a 2:2:1 v/v/v ratio. Our findings indicate that the effective mixing of these solvents enhances the overall polarity, thereby substantially reducing self-interactions.

In conjunction with commercially available gold and carbon inks for printing interconnects and electrode substrates, we successfully demonstrated the large-scale and low-cost production of flexible multiplexed MIP/NiHCF-nanoparticle-based sensor arrays suitable for wearable and implantable applications (Fig. 3c, Supplementary Figs. 8 and 9, and Supplementary Table 1). Open circuit potential-electrochemical impedance spectroscopy (OCP-EIS) characterization of both the printed carbon substrate and the printed MIP/NiHCF-nanoparticle-based electrodes, before and after target recognition, demonstrated decreased impedance after nanoparticle printing

https://doi.org/10.1038/s41563-024-02096-4

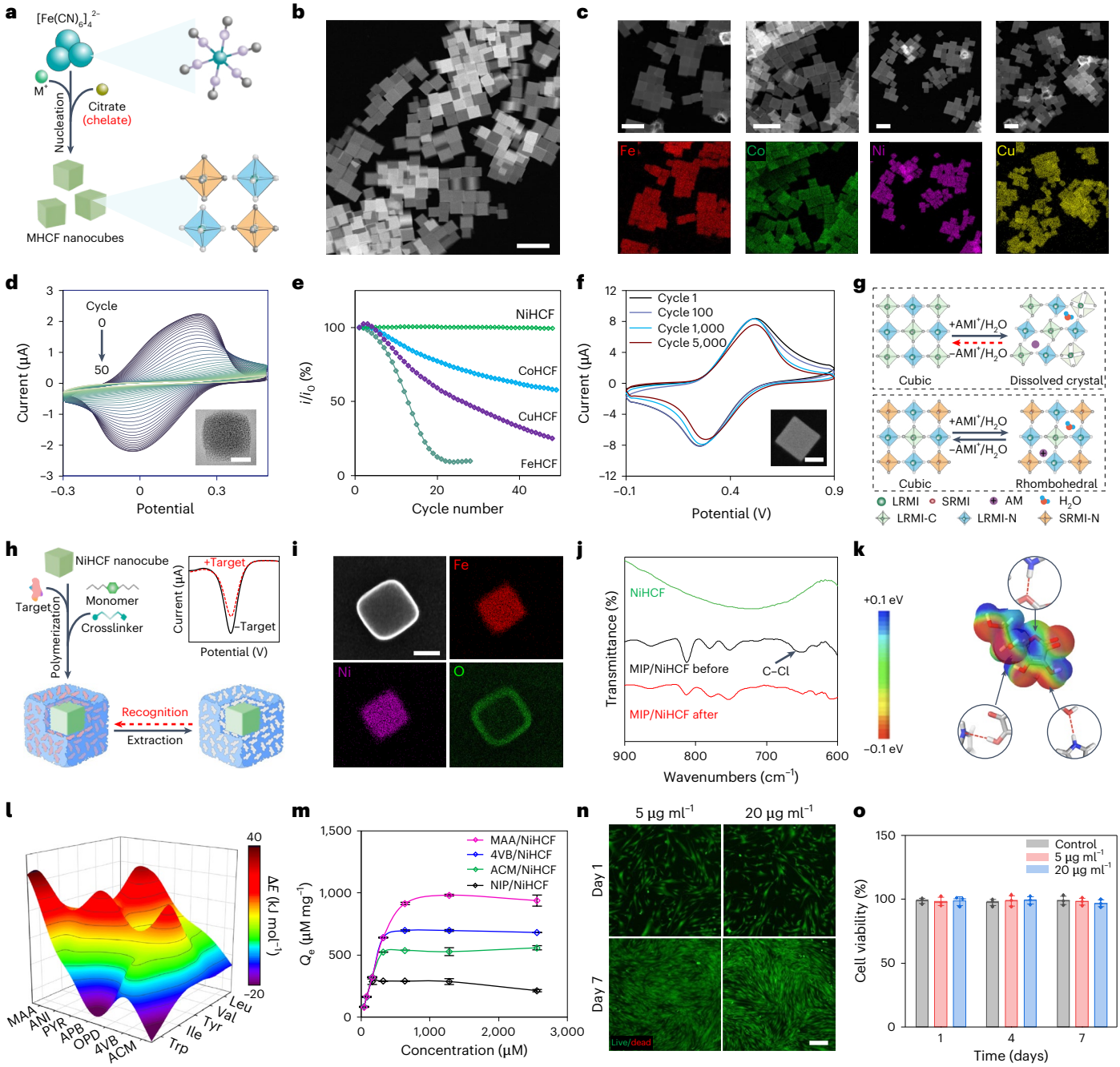

Fig. 2 | Design and characterization of dual-function core–shell nanoparticles for target recognition and signal transduction. a, Schematic of chelate-assisted synthesis of PBAs as the core. **b**, DF-STEM image of synthesized NiHCF cubic nanoparticles. Scale bar, 200 nm. **c**, DF-STEM images (top) and EDS mapping (bottom) of FeHCF, CoHCF, NiHCF and CuHCF cubic nanoparticles. Scale bars, 200 nm. **d**, CV scans of FeHCF in artificial sweat over 50 cycles. Inset: TEM image of FeHCF after 50 cycles. Scale bar, 50 nm. **e**, Changes in the CV oxidation peak current of FeHCF, CoHCF, NiHCF and CuHCF under repetitive CV scans. i and i_0 represent the peak current height and the initial first scan value, respectively. **f**, CV of NiHCF nanoparticles at the 1st, 100th, 1,000th and 5,000th scans. Inset: DF-STEM image of NiHCF after 5,000 cycles. Scale bar, 50 nm. **g**, Ion-intercalation mechanism of MHCFs. AMI, alkali-metal ion; SRMI, small-radius metal ion; LRMI, large-radius metal ion; C, carbon; N, nitrogen. **h**, Schematic of solution synthesis of core–shell MIP/NiHCF nanoparticles, and the electrochemical sensing mechanism. **i**, DF-STEM (top left) and EDS characterization of core–shell MIP/NiHCF nanoparticle. The images are representative of three independent experiments. Scale bar, 50 nm. **j**, FTIR characterization of NiHCF and MIP/NiHCF nanoparticles before and after target (AA) extraction. **k**, Electrostatic potential of an AA molecule. **l**, Binding-energy map showing differences between AA-monomer and interference-monomer complexes. ΔE, binding energy difference; ANI, aniline; APB, 3-aminophenylboronic acid; OPD, *o*-phenylene-diamine; PYR, pyrrole. **m**, Maximum adsorption amount (Q_e) of AA with core–shell nanoparticles prepared from different monomers in 40–2,500 μM AA. NIP, non-imprinted polymer. Error bars represent the s.d. of the mean from three measurements. **n**, Live (green)/dead (red) images of HDFs after 1 day and 7 days of culture with varying MIP/NiHCF nanoparticle concentrations. Scale bar, 200 μm. **o**, Cell viability analysis over 7 days with different MIP/NiHCF nanoparticle concentrations. Error bars represent the s.d. of the mean from three measurements.

https://doi.org/10.1038/s41563-024-02096-4

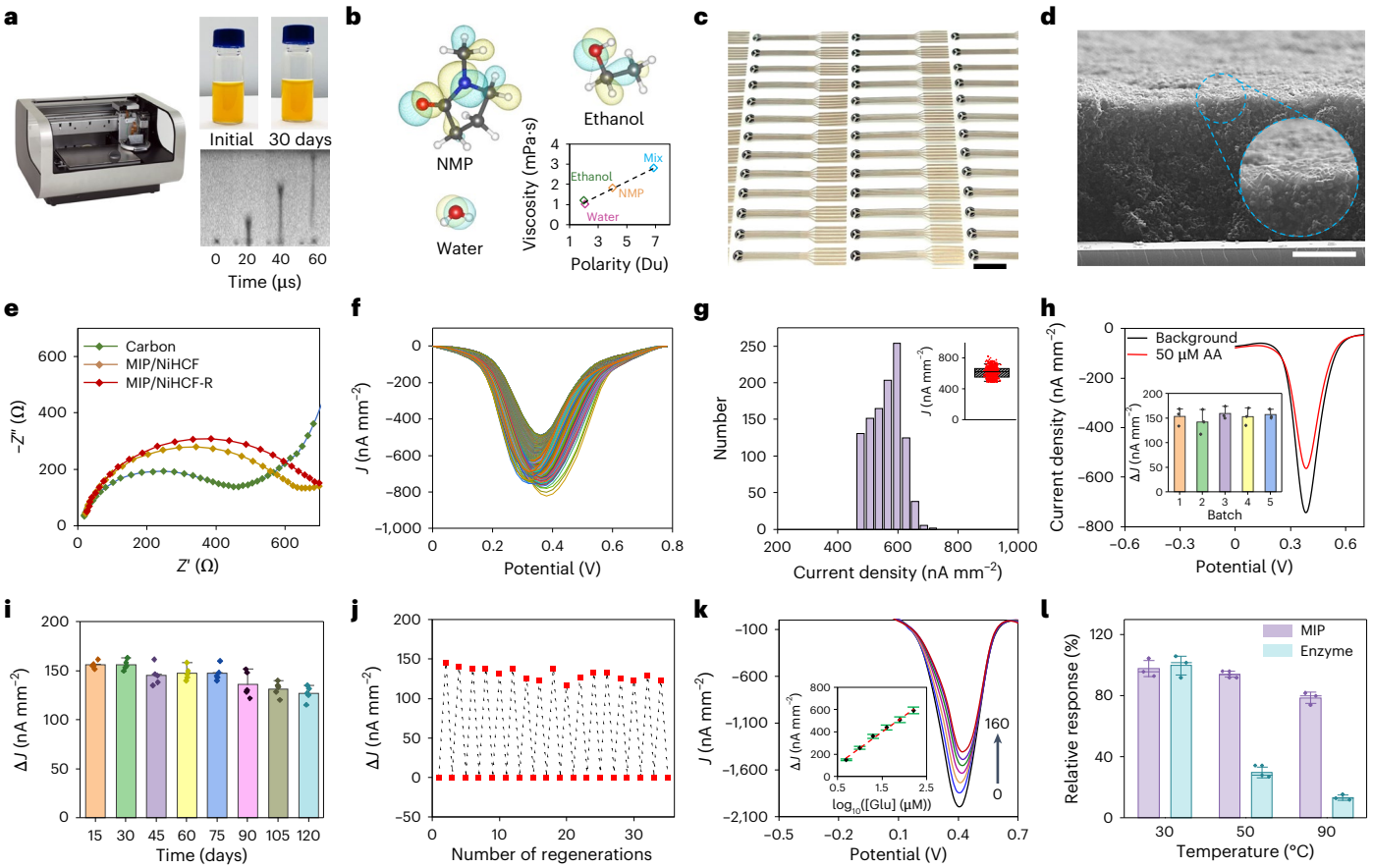

Fig. 3 | Characterization of the fully inkjet-printed MIP/NiHCF-nanoparticle-based electrochemical biosensors. a, High-resolution inkjet printing of biosensors with a customized MIP/NiHCF nanoparticle ink. Left: inkjet printer; top right: engineered highly stable MIP/NiHCF nanoparticle ink before and after a 30-day storage period; bottom right: 5 pl ink droplet ejection from the printer head during printing. **b**, HOMOs of the solvent molecules used to disperse MIP/NiHCF nanoparticles; bottom right: calculated polarity versus tested viscosity of the inks with 5 mg ml^{-1} nanoparticles. Mix, water/ethanol/NMP (2:2:1, v/v/v). **c**, Optical image of multiplexed sensor patch arrays fabricated via mass-producible inkjet printing. Scale bar, 2 cm. **d**, SEM image of a cross-section view of an inkjet-printed carbon-MIP/NiHCF nanoparticle electrode. Scale bar, 1 μm. **e**, OCP-EIS characterization of an inkjet-printed carbon electrode, an MIP/NiHCF nanoparticle electrode and an MIP/NiHCF nanoparticle–carbon electrode after target recognition (MIP/NiHCF-R). Z, Z' and Z'' represent impedance, resistance and reactance, respectively. **f**,**g**, Differential pulse voltammograms (**f**) and the corresponding distribution of peak current densities (**g**) of inkjet-printed sensor electrodes (n = 1,078) in artificial sweat. J, current density. **h**, Differential pulse voltammograms of the MIP/NiHCF-nanoparticle-based AA sensors from five different batches tested in PBS containing 50 μM AA. Inset: corresponding peak height current densities. ΔJ, peak height current density difference. Error bars represent the s.d. of the mean from five sensors. **i**, Room-temperature storage stability of the MIP/NiHCF-nanoparticle-based AA sensors for detecting 50 μM AA. The different colours represent sensors incubated under various temperatures. **j**, In situ regeneration of the MIP/NiHCF-nanoparticle-based AA sensors in artificial sweat. Regeneration of the sensing electrode was realized by applying −0.3 V for 60 s. **k**, Differential pulse voltammograms of the MIP/NiHCF-nanoparticle-based glucose sensor for glucose detection. Inset: calibration plot with a linear fit. Error bars represent the s.d. of the mean from three sensors. **l**, Relative response of MIP/NiHCF-nanoparticle-based glucose sensors and enzymatic glucose sensors at room temperature after baking at 30 °C, 50 °C and 90 °C for 2 h. Error bars represent the s.d. of the mean from five sensors.

and increased impedance after target molecule binding, confirming the successful preparation of the MIP/NiHCF-nanoparticle-based biosensors (Fig. 3e and Supplementary Fig. 10).

The printed MIP/NiHCF-nanoparticle-based biosensors exhibit high reproducibility due to the inherent simplicity and precision of the sensor manufacturing process. This process involves a one-step inkjet printing of a nanoparticle film with a dual function of target recognition and signal transduction. Electrochemical characterization of 1,078 such printed MIP/NiHCF-nanoparticle-based AA sensors demonstrated consistently narrow distributions of the reduction peak height in the DPV voltammograms with a mean peak current of 611.9 ± 67.9 nA mm^{-1} in artificial sweat (Fig. 3f,g), indicating the high quality of printing and the resulting robust performance of the sensors. In addition, printed MIP/NiHCF-nanoparticle-based AA sensors from different fabrication batches showed highly consistent electrode characteristics along with uniform NiHCF redox signal changes when detecting physiologically relevant AA levels, confirming the high reproducibility achieved in sensor manufacturing (Fig. 3h and Supplementary Fig. 11). Cross-sectional scanning electron microscopy (SEM) and surface metrology characterizations of the printed working electrodes reveal a uniform and dense packed arrangement of the printed core–shell nanocubes on the carbon substrate (Fig. 3d and Supplementary Fig. 12); four layers of printed nanoparticles with a thickness and roughness of 203 nm and 216 nm, respectively, showed optimal electrochemical sensor performance (Supplementary Figs. 12 and 13). To enhance the sensor response, we conducted additional optimizations in both MIP shell composition and target incubation time, as illustrated in Supplementary Fig. 14. The printed AA sensor demonstrated high selectivity to other main body fluid analytes with physiologically relevant concentrations (Supplementary Fig. 15 and Supplementary Table 2). These sensors demonstrated stable performance in biologically relevant sample matrices, including PBS, sweat and serum, indicating their high anti-biofouling properties (Supplementary Figs. 16 and 17).

Compared to enzymatic or other affinity-based biosensors[33,34], our printed MIP/NiHCF-nanoparticle-based sensors offer evident advantages in terms of their room-temperature storage durability, continuous usability and thermal resilience under harsh environments. The printed MIP/NiHCF-nanoparticle-based AA sensors demonstrated high stability by retaining over 80% of their sensitivity after a four-month storage period at room temperature (Fig. 3i). Unlike other bioaffinity sensors based on antibodies and DNA receptors that are usually one-time use, the printed MIP/NiHCF-nanoparticle-based sensors can be easily regenerated in situ by applying an optimal electrochemical potential to remove the bound target molecules, enabling long-term, stable, selective and continuous biomarker analysis in biofluids (Fig. 3j and Supplementary Figs. 18 and 19). Moreover, the printed sensor exhibits superior performance under extreme environments (for example, high temperature), in which target-binding receptors based on proteins (for example, enzymes and antibodies) or nucleic acids (for example, DNA or aptamers) are prone to denaturation. To demonstrate the superior thermal stability of our MIP/NiHCF-nanoparticle-based sensors over traditional enzymatic sensors for detecting the same target analyte, we compared the performance of the MIP/NiHCF-nanoparticle-based glucose sensors (Fig. 3k) with that of enzymatic electrochemical glucose sensors. Glucose was chosen due to the availability of relevant enzymes. Our results showed that the MIP/NiHCF sensor retained 76% of its analytical performance even after exposure to a high temperature of 90 °C, whereas the enzymatic sensor experienced an 84% signal loss under the same conditions (Fig. 3l).

Evaluation of core–shell nanoparticles for wearable metabolic and nutritional monitoring

The printed MIP/NiHCF-nanoparticle-based biosensors exhibit high performance, making them well suited for wearable and implantable applications in personalized healthcare, particularly for monitoring long COVID. Long COVID, stemming from previous COVID-19 infection, has a prolonged impact on individuals' health and well-being. A panel of biomarkers, including AA, CK and Trp, were chosen based on their association with long COVID (Fig. 4a). AA levels are critical for immune function and symptom mitigation[35,36]; elevated CK levels, signalling kidney impairment, are often seen in fatigue and muscle weakness[37,38]; and Trp disruptions contribute to mood and cognitive issues[39,40]. Monitoring these metabolic biomarkers non-invasively has the potential to facilitate tailored care and enhance our understanding and management of long COVID[41,42].

To realize automated non-invasive biomarker monitoring in situ, we engineered a wearable sweat sensor patch that features three inkjet-printed MIP/NiHCF-nanoparticle-based sensors, specially designed for quantifying AA, CK and Trp, alongside a pair of carbon electrodes coated with carbachol gels for on-demand autonomous sweat induction at rest via iontophoresis (Fig. 4b). Augmenting these features is a multi-inlet microfluidic module equipped with an outlet, facilitating efficient sweat collection and refreshment. Concurrently, flexible electronic circuitry was devised for signal processing and wireless data transmission (Fig. 4c). The resulting wearable microfluidic sensor patch autonomously samples induced sweat with high temporal resolution (Fig. 4d). The printed wearable sensors exhibit highly reproducible sensor performance with log-linear responses between the changes of DPV peak height current density and analyte concentration (Fig. 4e and Supplementary Figs. 20 and 21). Moreover, these sensors are mechanically flexible, and demonstrated stable sensor performance during 1,200 cycles of mechanical bending, making them suitable for practical on-body use during daily activities (Fig. 4f). The fully integrated sensor patch conformally adheres to the skin and could function as a 'smart ring' or 'smart band' for wireless and continuous health monitoring (Fig. 4g and Supplementary Figs. 22–24).

To investigate the potential of sweat AA, CK and Trp as non-invasive indicators for long COVID assessment, pilot studies were performed in human participants to scrutinize the correlations between serum and sweat AA, CK and Trp. Positive Pearson correlation coefficients of 0.87, 0.81 and 0.86 were identified for AA, CK and Trp, respectively, indicating close associations between their levels in sweat and serum (Fig. 4h). Subsequent human studies were conducted to evaluate the wearable sensors in healthy participants and long COVID patients under fasting conditions by simultaneously monitoring AA, CK and Trp levels in situ (Fig. 4i–k and Supplementary Table 3). Compared with the healthy participants, long COVID patients in this study exhibited notably higher CK levels and lower AA and Trp (Fig. 4l), consistent with previous reports on their blood counterparts[38,40,43]. Considering the profound influence of dietary intake on the temporary AA and Trp levels, we also validated the wearable sensor system through a meal challenge (Fig. 4m–p). Rapid increases in the levels of sweat AA and Trp were observed in all participants following food intake, while CK levels remained relatively stable, which was attributed to the fact that CK, a by-product of the dehydration and breakdown of creatine in muscles, is not immediately influenced by short-term nutrient intake. Meanwhile, rising AA and Trp levels in sweat were observed from all three subjects after AA and Trp supplement intake (Supplementary Fig. 25). These findings highlight the potential of the MIP/NiHCF-nanoparticle-based wearable sensor system as a powerful tool for capturing real-time fluctuations in sweat metabolic biomarkers, providing valuable insights for future fundamental investigations into long COVID and various other physiological conditions.

Evaluation of core–shell nanoparticles in wearable/implantable TDM

Another promising application of the printed core–shell nanoparticle-based sensor is real-time TDM. Personalizing dosing to maintain drug concentrations within the therapeutic window is crucial for effective pharmacotherapy, maximizing effectiveness while minimizing toxicity[44,45] (Fig. 5a). Traditional TDM protocols require invasive blood draws and laboratory analyses, resulting in delayed intervention and a suboptimal temporal resolution[4]. Wearable and implantable biosensors offer a solution by enabling continuous real-time drug monitoring and dose personalization (Fig. 5b). In this regard, we developed MIP/NiHCF-nanoparticle-based sensors capable of selectively quantifying three anticancer immunosuppressive drugs: CY, BU and MPA (Supplementary Fig. 26). These drug sensors demonstrated log-linear relations between the DPV peak height current density and analyte concentration with sensitivities of 185.02, 253.06 and 536.07 nA mm^{-2} per decade of concentration for CY (Fig. 5c), BU (Fig. 5d) and MPA (Fig. 5e), respectively.

To validate the accuracy of the wearable biosensors for analysing drug levels, sweat samples from hospitalized cancer patients receiving CY or BU were analysed with the sensors and the gold standard liquid chromatography–tandem mass spectrometry (LC–MS/MS) (Supplementary Fig. 27 and Supplementary Table 4). The results revealed robust correlations, with Pearson correlation coefficients of 0.92 and 0.98 for the measurement of CY and BU concentrations (Fig. 5f), respectively, suggesting the reliability of the sensor measurements. Further, on-body assessment of the wearable biosensors was performed on two patients diagnosed with acute myeloid leukaemia (AML) who received CY and two patients diagnosed with sickle cell disease (SCD) and AML, respectively, who received treatment with BU (Fig. 5g–i). As expected, sweat BU and CY levels monitored by the wearable sensors followed similar trends as the plasma concentration–time curves after respective drug infusions, indicating the high potential of wearable sweat drug monitoring for clinical management beyond traditional hospital settings.

Although wearable sweat sensors offer an enticing prospect for non-invasive monitoring of circulating drug levels in patients, implantable biosensors, despite their invasive nature, present distinct advantages in terms of sensing accuracy, tumour-specific pharmacokinetics

https://doi.org/10.1038/s41563-024-02096-4

Fig. 4 | Evaluation of the printed MIP/NiHCF-nanoparticle-based biosensor for wearable long COVID and nutritional monitoring. a, Schematic of wearable long COVID monitoring through non-invasive monitoring of AA, CK and Trp using a wearable sensor. **b**, Schematic design of a wearable sweat sensor patch for sweat induction, microfluidic sweat sampling and multiplexed analysis. Segments 1–3 represent working electrodes printed with MIP/NiHCF nanoparticles for the detection of AA, CK and Trp, respectively. **c**, Layered design of the flexible and wireless microfluidic wearable patch. Sections 1–8 represent plastic substrate interfacing with the FPCB (1), inkjet-printed electrodes and interconnects (2), the inkjet-printed MIP/NiHCF nanoparticle sensing layer (3), carbachol-loaded hydrogels (carbagels) (4), the reservoir layer (5), the inlet layer (6), the sweat accumulation layer (7) and the skin (8). **d**, Time-lapse images of microfluidic sampling of iontophoresis-induced sweat at rest using the wearable patch. Scale bar, 5 mm. **e**, Calibration plots of AA, CK and Trp in artificial sweat. Dashed lines represent linear-fit trendlines. Error bars represent the s.d. of the mean from three sensors. **f**, Sensing performance of the AA sensors over 1,200 bending cycles. Radius of bending curvature, 2.5 cm. Inset: sheet of printed sensor arrays under mechanical deformation. Scale bar, 2 cm. Error bars represent the s.d. of the mean from three patches. **g**, Photographs of a fully integrated wireless wearable patch worn on the finger and on the wrist. Scale bar, 1 cm. **h**, Correlation of serum and sweat AA ($n = 9$), CK ($n = 14$) and Trp ($n = 12$) levels. r, Pearson's correlation coefficient. **i**–**k**, On-body multiplexed sweat AA (**i**), CK (**j**) and Trp (**k**) analysis using the wearable sensors from three healthy participants and three participants with long COVID. **l**, Box plot of sweat AA, CK and Trp levels from the healthy and long COVID participates. Error bars represent the s.d. of the mean from 30 measurements on all three participants. **m**–**p**, Schematic of a human participant with protein and strawberry intake (**m**) and resulting on-body multiplexed AA (**n**), CK (**o**) and Trp (**p**) analysis using the wearable biosensors.

measurements and applicability for pharmacokinetic/pharmacodynamic studies in animal models[46]. To demonstrate the practical applications of our MIP/NiHCF nanoparticles in implantable sensing, we developed a printed implantable sensor array capable of simultaneously monitoring three immunosuppressants—CY, BU and MPA—in interstitial fluid in vivo within living animals (Fig. 5j and Supplementary Fig. 28). In vivo assessment of the implantable sensor patch for pharmacokinetic studies was carried out in mice through intravenous injection of drugs at varying doses. The results demonstrated an observed dose-dependent increase in the area under the concentration–time

https://doi.org/10.1038/s41563-024-02096-4

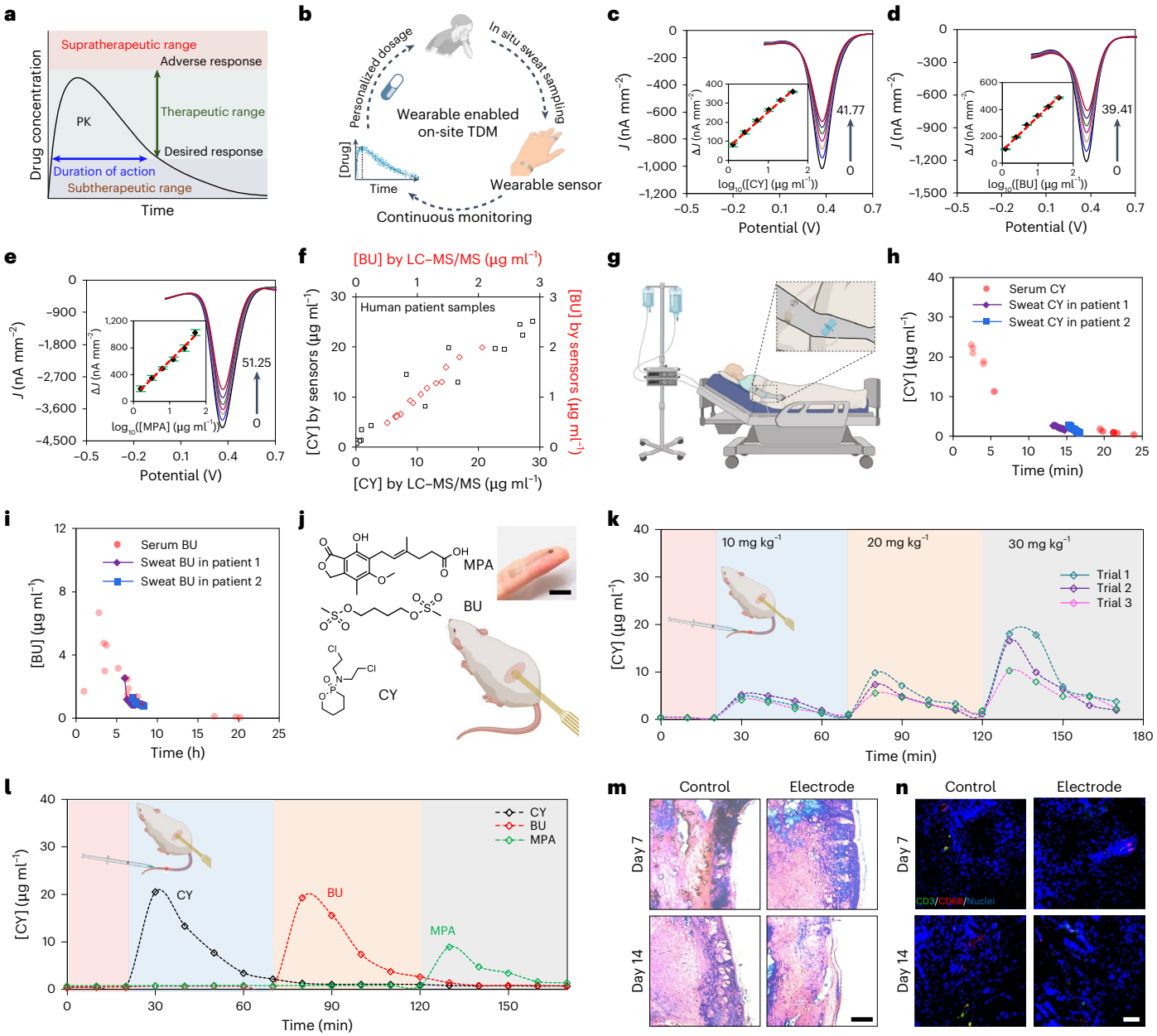

Fig. 5 | Evaluation of the wearable and implantable MIP/NiHCF-nanoparticle-based biosensor for real-time TDM. a, Temporal characteristics of drug effect and relationship to the therapeutic window. PK, pharmacokinetics. **b**, Schematic of the prospect of on-site clinical practice based on wearable-sensor-guided personalized medicine. **c**–**e**, DPV voltammograms of the printed MIP/NiHCF-nanoparticle-based CY (**c**), BU (**d**) and MPA (**e**) sensors. Insets: calibration plots with a linear fit. The different colour traces represent varying concentrations of the targets. Error bars represent the s.d. of the mean from three sensors. **f**, Validation of CY ($n = 15$) and BU ($n = 14$) biosensors against LC–MS/MS for analysing human sweat samples from hospitalized cancer patients undergoing chemotherapy. **g**, Schematic illustration of in situ personalized TDM on cancer patients using the printed wearable sensor. **h**, CY levels obtained by the wearable sweat sensors from two cancer patients with diagnosed AML after CY infusion. **i**, BU obtained by the wearable sweat sensors from two cancer patients with diagnosed SCD and AML, respectively, after BU infusion. **j**, Schematic of an implantable array for multiplexed BU, CY and MPA monitoring. Top right: photograph of a flexible printed MIP/NiHCF-nanoparticle-based implantable sensor patch designed for in vivo TDM in a mouse model. Scale bar, 1 cm. **k**, CY levels monitored by the implantable CY sensors in three mice after lateral tail vein injection of different doses of CY. **l**, CY, BU and MPA levels monitored by the implantable sensor arrays in three mice after the intravenous injection of CY, BU and MPA (30 mg kg^{-1}). **m**, Haematoxylin and eosin staining of implantable patch with the surrounding mouse tissue after 4 days and 14 days of implantation. Scale bar, 200 μM. **n**, Fluorescent immunohistochemical analysis of subcutaneously implanted sensor patch at days 4 and 14. Green, red and blue represent lymphocyte (CD3), macrophages (CD68) and cell nuclei, respectively. The images are representative of three independent experiments. Scale bar, 100 μm.

curve corresponding to CY dosages, as depicted in Fig. 5k. Additionally, the multiplexed implantable sensor demonstrated selective recognition capabilities for distinct drugs administered at disparate time points (Fig. 5l). Considering the crucial importance of in vivo cytocompatibility for implantable devices, immunohistological and immunofluorescent staining of the subcutaneously implanted sensor patch was performed in mice. The results demonstrated minimal presence of leukocyte (CD3) and macrophage (CD68) antigens after 14 days, confirming the high cytocompatibility of the implantable patch (Fig. 5m,n). For long-term implantable applications, incorporating a porous polyurethane layer on top of the sensing electrode can effectively mitigate the biostress induced by an applied voltage (Supplementary Fig. 29).

This approach maintains comparable sensing performance while substantially enhancing the long-term operation stability in vivo and in biofluids with high reproducibility (Supplementary Figs. 30–32).

Outlook

We demonstrated in this work a core–shell nanoparticle consisting of an MIP shell and a redox-active core based on PBAs that offers selective target recognition and effective signal transduction. This dual-function nanoparticle enables mass production of flexible biosensors with high selectivity, high operating stability and long shelf life, addressing key challenges in wearable and implantable biosensors, including limited detectable targets, scalability and poor long-term stability. In addition to the metabolic and therapeutic drug monitoring we demonstrate here, this printable core–shell nanoparticle technology can be adapted for diverse health monitoring applications. Further enhancements in sensitivity and in vivo stability support the practical deployment of these devices, enabling high-quality, scalable biosensors for global healthcare markets. The extensive data collected will drive fundamental and clinical insights, marking a step toward the transformative impact of wearable and implantable biosensors in healthcare.

Online content

Any methods, additional references, Nature Portfolio reporting summaries, source data, extended data, supplementary information, acknowledgements, peer review information; details of author contributions and competing interests; and statements of data and code availability are available at https://doi.org/10.1038/s41563-024-02096-4.

References

1. Suhre, K. et al. Human metabolic individuality in biomedical and pharmaceutical research. *Nature* **477**, 54–60 (2011).
2. Amoozgar, Z., Jaymand, M. & Jahanban-Esfahlan, R. Editorial: Circulating molecular biomarkers: next-generation tools for monitoring minimal residual disease in cancer patients. *Front. Oncol.* **13**, 1226974 (2023).
3. Wang, T. J. et al. Metabolite profiles and the risk of developing diabetes. *Nat. Med.* **17**, 448–453 (2011).
4. Ates, H. C. et al. On-site therapeutic drug monitoring. *Trends Biotechnol.* **38**, 1262–1277 (2020).
5. Kim, J., Campbell, A. S., de Ávila, B. E.-F. & Wang, J. Wearable biosensors for healthcare monitoring. *Nat. Biotechnol.* **37**, 389–406 (2019).
6. Li, J. et al. A tissue-like neurotransmitter sensor for the brain and gut. *Nature* **606**, 94–101 (2022).
7. Ates, H. C. et al. End-to-end design of wearable sensors. *Nat. Rev. Mater.* **7**, 887–907 (2022).
8. Min, J. et al. Skin-interfaced wearable sweat sensors for precision medicine. *Chem. Rev.* **123**, 5049–5138 (2023).
9. Bariya, M., Nyein, H. Y. Y. & Javey, A. Wearable sweat sensors. *Nat. Electron.* **1**, 160–171 (2018).
10. Tehrani, F. et al. An integrated wearable microneedle array for the continuous monitoring of multiple biomarkers in interstitial fluid. *Nat. Biomed. Eng.* **6**, 1214–1224 (2022).
11. Sempionatto, J. R., Lasalde-Ramírez, J. A., Mahato, K., Wang, J. & Gao, W. Wearable chemical sensors for biomarker discovery in the omics era. *Nat. Rev. Chem.* **6**, 899–915 (2022).
12. Lee, H. et al. A graphene-based electrochemical device with thermoresponsive microneedles for diabetes monitoring and therapy. *Nat. Nanotechnol.* **11**, 566–572 (2016).
13. Koydemir, H. C. & Ozcan, A. Wearable and implantable sensors for biomedical applications. *Annu. Rev. Anal. Chem.* **11**, 127–146 (2018).
14. Luo, Y. et al. Technology roadmap for flexible sensors. *ACS Nano* **17**, 211–5295 (2023).
15. Heikenfeld, J. et al. Accessing analytes in biofluids for peripheral biochemical monitoring. *Nat. Biotechnol.* **37**, 407–419 (2019).
16. Flynn, C. D. et al. Biomolecular sensors for advanced physiological monitoring. *Nat. Rev. Bioeng.* **1**, 560–575 (2023).
17. Ye, C. et al. A wearable aptamer nanobiosensor for non-invasive female hormone monitoring. *Nat. Nanotechnol.* **19**, 330–337 (2024).
18. Jiang, Y. et al. Recent advances of Prussian blue-based wearable biosensors for healthcare. *Anal. Chem.* **94**, 297–311 (2022).
19. Kim, J. et al. Wearable bioelectronics: enzyme-based body-worn electronic devices. *Acc. Chem. Res.* **51**, 2820–2828 (2018).
20. Yu, Y. et al. All-printed soft human–machine interface for robotic physicochemical sensing. *Sci. Robot.* **7**, eabn0495 (2022).
21. Singh, S., Wang, J. & Cinti, S. Review—an overview on recent progress in screen-printed electroanalytical (bio)sensors. *ECS Sens.* **1**, 023401 (2022).
22. Wang, M. et al. A wearable electrochemical biosensor for the monitoring of metabolites and nutrients. *Nat. Biomed. Eng.* **6**, 1225–1235 (2022).
23. BelBruno, J. J. Molecularly imprinted polymers. *Chem. Rev.* **119**, 94–119 (2019).
24. Karyakin, A. A. Prussian blue and its analogues: electrochemistry and analytical applications. *Electroanalysis* **13**, 813–819 (2001).
25. Keßler, S., González-Rubio, G., Reinalter, E. R., Kovermann, M. & Cölfen, H. Synthesis of nickel hexacyanoferrate nanocubes with tuneable dimensions via temperature-controlled Ni^{2+}-citrate complexation. *Chem. Commun.* **56**, 14439–14442 (2020).
26. Peng, J. et al. Prussian blue analogues for sodium-ion batteries: past, present, and future. *Adv. Mater.* **34**, 2108384 (2022).
27. Ying, S. et al. Synthesis and applications of Prussian blue and its analogues as electrochemical sensors. *ChemPlusChem* **86**, 1608–1622 (2021).
28. Zhang, Z. et al. Lithiated Prussian blue analogues as positive electrode active materials for stable non-aqueous lithium-ion batteries. *Nat. Commun.* **13**, 7790 (2022).
29. Yi, H. et al. Structure and properties of Prussian blue analogues in energy storage and conversion applications. *Adv. Funct. Mater.* **31**, 2006970 (2021).
30. Xu, C. et al. A physicochemical-sensing electronic skin for stress response monitoring. *Nat. Electron.* **7**, 168–179 (2024).
31. *Cyclophosphamide. NIST Chemistry WebBook* SRD 69 (National Institute of Standards and Technology, accessed 15 December 2024); https://webbook.nist.gov/cgi/inchi?ID=C50180&Mask=80
32. Mukasa, D. et al. A computationally assisted approach for designing wearable biosensors toward non-invasive personalized molecular analysis. *Adv. Mater.* **35**, 2212161 (2023).
33. Wang, J. Electrochemical biosensors: towards point-of-care cancer diagnostics. *Biosens. Bioelectron.* **21**, 1887–1892 (2006).
34. Newman, J. D. & Setford, S. J. Enzymatic biosensors. *Mol. Biotechnol.* **32**, 249–268 (2006).
35. Vollbracht, C. & Kraft, K. Feasibility of vitamin C in the treatment of post viral fatigue with focus on long COVID, based on a systematic review of IV vitamin C on fatigue. *Nutrients* **13**, 1154 (2021).
36. Izzo, R. et al. Combining L-arginine with vitamin C improves long-COVID symptoms: the LINCOLN survey. *Pharmacol. Res.* **183**, 106360 (2022).
37. Alfano, G. et al. Twenty-four-hour serum creatinine variation is associated with poor outcome in the novel coronavirus disease 2019 (COVID-19) patients. *Kidney Res. Clin. Pract.* **40**, 231–240 (2021).
38. Bowe, B., Xie, Y., Xu, E. & Al-Aly, Z. Kidney outcomes in long COVID. *J. Am. Soc. Nephrol.* **32**, 2851–2862 (2021).
39. Eroğlu, İ., Eroğlu, B. Ç. & Güven, G. S. Altered tryptophan absorption and metabolism could underlie long-term symptoms in survivors of coronavirus disease 2019 (COVID-19). *Nutrition* **90**, 111308 (2021).

40. Al-Hakeim, H. K., Khairi Abed, A., Rouf Moustafa, S., Almulla, A. F. & Maes, M. Tryptophan catabolites, inflammation, and insulin resistance as determinants of chronic fatigue syndrome and affective symptoms in long COVID. *Front. Mol. Neurosci.* **16**, 1194769 (2023).
41. Davis, H. E., McCorkell, L., Vogel, J. M. & Topol, E. J. Long COVID: major findings, mechanisms and recommendations. *Nat. Rev. Microbiol.* **21**, 133–146 (2023).
42. Chan, H. Y. Wearable devices for long COVID: prospects, challenges and options. *Asian Bioeth. Rev.* **16**, 757–769 (2024).
43. Vollbracht, C. & Kraft, K. Oxidative stress and hyper-inflammation as major drivers of severe COVID-19 and long COVID: implications for the benefit of high-dose intravenous vitamin C. *Front. Pharmacol.* **13**, 899198 (2022).
44. Kang, J.-S. & Lee, M.-H. Overview of therapeutic drug monitoring. *Korean J. Intern. Med.* **24**, 1–10 (2009).
45. Mueller-Schoell, A. et al. Therapeutic drug monitoring of oral targeted antineoplastic drugs. *Eur. J. Clin. Pharmacol.* **77**, 441–464 (2021).
46. Gray, M. et al. Implantable biosensors and their contribution to the future of precision medicine. *Vet. J.* **239**, 21–29 (2018).

Methods

Materials and reagents

Creatinine, tyrosine, uric acid, valine, vitamin B_6, vitamin D_3, vitamin E, glucose, silver nitrate, iron(III) chloride and lactate were purchased from Alfa Aesar. AA, alanine, ammonium formate (>99%), choline chloride, citrulline, histidine, leucine, lysine, methionine, nicotinic acid, ornithine, pantothenic acid calcium salt, phenylalanine, riboflavin, serine, thiamine, threonine, Trp, iron(II) acetate, cobalt(II) acetate tetrahydrate, nickel(II) acetate tetrahydrate, copper(II) acetate hydrate, potassium hexacyanoferrate(III), MAA, acrylamide (ACM), 4-vinylbenzoic acid (4VB), CY, MPA, ethylene glycol dimethylacrylate, azobisisobutyronitrile and acetic acid were purchased from Sigma-Aldrich. Potassium ferricyanide was purchased from Acros Organics. Trisodium citrate dihydrate, methanol, glycine, glutamic acid and acetonitrile were of HPLC grade and along with NMP were purchased from Thermo Fisher Scientific. Medical adhesives were purchased from 3M and Adhesives Research. Polyimide films with a thickness of 75 µm were purchased from DuPont. Polyethylene terephthalate (PET) films (12 µm thick) were purchased from McMaster-Carr. BU and busulfan-D_8 (BU-D_8) were purchased from CND Isotopes. CY was purchased from Sigma-Aldrich. 4-Ketocyclophosphamide (Keto-CY), deschloroethylcyclophosphamide (DCCY), carboxyethylphosphoramide mustard (CEPM), cyclophosphamide-D_4 (CY-D_4) and carboxyethylphosphoramide mustard-D_4 (CEPM-D_4) were purchased from Toronto Research Chemicals. Analyte-free human plasma for preparation of standards and quality controls (QC) was purchased from Innovative Research. Artificial sweat was purchased from RICCA Chemical.

Synthesis of the PBA (FeHCF, CoHCF, NiHCF and CuHCF) nanoparticles

For the synthesis of PBA nanoparticles, transition metal acetates (iron(II) acetate, cobalt(II) acetate tetrahydrate, nickel(II) acetate tetrahydrate and copper(II) acetate hydrate) (600 µM) and trisodium citrate dihydrate (chelating agent, 900 µM) were dissolved in 20 ml of water and injected (20.0 ml min^{-1}) into 20 ml of potassium hexacyanoferrate(III) (400 µM) aqueous solution. The reaction was conducted at room temperature (22 °C) for 24 h, followed by centrifugation at 18,000 relative centrifugal force (rcf) for 10 min using an Eppendorf 5424 centrifuge. After discarding the supernatants, the resulting nanoparticles were washed four times with 60 ml of deionized water. Subsequently, they were dried in a vacuum oven at 40 °C overnight and stored at 4 °C for future use.

Core–shell MIP/NiHCF nanoparticle synthesis and characterization

All MIP/NiHCF nanoparticles were synthesized via bulk polymerization using a standardized experimental procedure, with slight variations depending on the specific type of MIP nanoparticle. In this method, the target molecule was introduced at concentrations ranging from 1 to 20 mM, depending on optimization requirements. Simultaneously, 20 mM of the selected monomer (for example, MAA, ACM or 4VB) was added into 10 ml of a 1:4 deionized water/methanol (v/v) mixture containing 15 mg well-dispersed NiHCF nanoparticles and stirred until complete dissolution occurred. Subsequently, 40 mM of ethylene glycol dimethylacrylate, serving as the cross-linker, was added and mixed until dissolved. After being purged with nitrogen for 10 min, the resulting mixture was stirred at room temperature for 24 h. Following this, 25 mM of azobisisobutyronitrile, the initiator, was introduced into the solution and the container was purged with nitrogen for 10 min at low pressure to avoid decarboxylation. Polymerization was initiated by placing the reaction vessel in a 40 °C water bath for 5 h. Template removal was achieved by immersing the polymer particles in a solution containing 5 ml of acetic acid and methanol in a 7:3 v/v ratio and stirring overnight. The next day, the particle suspension underwent three water-washing steps, each at 10,000 rcf for 2 min, followed by a final methanol wash at 10,000 rcf for 2 min. Finally, the washed core–shell MIP/NiHCF nanoparticles were dried at 30 °C in a vacuum oven until completely dry, making them ready for subsequent testing and analysis.

The morphological features and material attributes were systematically assessed through various instruments. Transmission electron microscopy (TEM) analysis was conducted with a Talos S-FEG FEI instrument; scanning electron microscopy (SEM) was performed with a Nova Nano SEM 450. MIP/NiHCF nanoparticles with different monomers were characterized with ultraviolet–visible spectroscopy (Thermo Scientific NanoDrop) to experimentally demonstrate the sensitivity and selectivity of the nanoparticles. The crystalline structures of the samples were characterized with a Rigaku Smartlab X-ray diffractometer with a Cu Kα radiation (λ = 1.5418 Å) source. The thickness and roughness of the printed MIP/NiHCF were measured by a profilometer (Dektak 3ST).

The cytocompatibility of MIP nanoparticles was examined by culturing with HDFs (cultured at 37 °C under 5% CO_2; cells were passaged at 70% confluency) using live/dead assay after prolonged coincubation (days 1–7) with different concentrations of nanoparticles (5 and 20 µg ml^{-1}).

Computationally assisted MIP optimization

To design MIP electrodes sensitive and selective to AA, we used the QuantumDock algorithm as described in our previous report[32]. We use QuantumDock's standard configurations for DFT simulations which include a B3LYP functional with a 6-31G**++ basis set and D3BJ dispersion corrections. We searched seven monomers for their potential sensitivity and selectivity against six potentially interfering molecules commonly found in sweat.

Design of the MIP/NiHCF nanoparticle ink

The nanoparticle inks were computationally optimized to mitigate the self-interactions of MIP/NiHCF nanoparticles, and hence the nanoparticles were evenly dispersing in the ink solution. The dipole moment was used as a proxy for the solvent's capacity to interact with sensing particles and hinder self-interaction. Molecular properties were calculated using DFT in PySCF[47] using the B3LYP functional and a 6-31 basis set. HOMO orbitals were calculated to visualize the solvent molecule polarity for diethylene glycol diethyl ether, isopropanol, water, ethanol, butanol and NMP. Similarly, the dipole moment of each solvent was calculated using this method. Solvent mixtures such as our optimized solvent mixture were simulated by optimizing the mixture system via Universal Force Field in the Avogadro software package, followed by the aforementioned B3LYP 6-31G DFT simulation.

Design of PBA crystal structure

We used the Quantum Espresso package to perform first-principles calculations on crystals of PBA (metal hexacyanoferrate (MHCF)). The free energy of each crystal structure was calculated by first relaxing the crystal structure, allowing the structure to obtain an optimized geometry. We used a plane-wave cut-off energy of 50 Ry and a charge density cut-off of 400 Ry. Electron occupations were treated using Marzari–Vanderbilt smearing with a smearing width of 0.02 Ry. Spin polarization was enabled, with initial magnetizations for the first two atom types set at 0.5 while using the unified pseudopotential format.

Fabrication and characterization of sensor patches via inkjet printing

The process for fabricating the inkjet-printed wearable sensor patch is depicted in Supplementary Fig. 22. Initially, the PET substrate underwent a sequence of treatments, beginning with a thorough cleaning using isopropyl alcohol and subsequent drying with a compressed air flow. A 5 min O_2 plasma surface treatment was performed with Plasma Etch PE-25 (20–30 cm^3 min^{-1} O_2, 100 W, 150–200 mtorr) to enhance the

surface hydrophilicity of the PET substrate. The multimodal sensor patch was manufactured through a meticulously optimized serial printing process. This involved the serial printing of multiple layers, including gold (utilized for interconnects, three layers), carbon (serving as both the counter-electrode and as a conductive layer for working electrodes, six layers), silver (reference electrode, two layers), SU-8 (used for encapsulation, three layers), and a four-layer assembly of target-selective core–shell MIP/NiHCF nanoparticles using an inkjet printer (DMP-2850, Fujifilm). The gold ink (10 wt%) was purchased from C-INK. Silver ink (25 wt%) and carbon ink (5 wt%) were purchased from NovaCentrix. All the three inks were used without further modification. The MIP/NiHCF nanoparticle ink was prepared by subjecting synthesized MIP/NiHCF nanoparticles at a concentration of 5 mg ml^{-1} to ultrasonic dispersion within a mixed solvent system comprising deionized water, ethanol and NMP in a 1:1:2 v/v/v ratio. Subsequently, the dispersion was filtered through a 0.45 µm filter to achieve the desired ink formulation. During the printing process, the temperature of the printing plate was maintained at 50 °C to ensure rapid vaporization of the ink solvent. Subsequently, the obtained patch was annealed at 90 °C. For the fabrication of the implantable sensor patch, an analogous procedure was followed, with the exception of utilizing a distinct pattern and different MIP nanoparticles. Additionally, we intentionally attached a porous polyurethane film onto the inkjet-printed implantable patch to mitigate the effects of biostress induced by applying voltage to electrochemically react with the redox probe. The porous polyurethane was constructed using a phase-separation method. Briefly, a polyurethane precursor dissolved in a mixed solvent of tetrahydrofuran and ethanol was drop-cast onto the water surface, where phase separation formed large-scale porous polyurethane membranes. These membranes were then retrieved and dried under ambient conditions (~3 h).

Electrochemical characterization of the electrodes and sensors

In vitro electrochemical analyses were conducted using CHI840D and CHI760 electrochemical workstations under ambient temperature in artificial sweat (1× PBS, pH 6.8, unless specified otherwise). DPV was used to assess the performance of the sensors. The following DPV conditions were used: voltage range, 0.8–0 V; incremental potential, 0.01 V; pulse amplitude, 0.05 V; pulse width, 0.05 s; pulse period, 0.5 s; sensitivity, 1×10^{-5} A V^{-1}. The stabilities of different MHCFs were characterized by long-term CV scanning.

DPV and OCP-EIS were performed to investigate the construction steps of the MIP nanoparticles in artificial sweat containing 2.0 mM $K_4Fe(CN)_6/K_3Fe(CN)_6$ (1:1) under the following conditions: potential range, 0.8–0 V; pulse width, 0.2 s; incremental potential, 4 mV; amplitude, 50 mV; frequency range, 0.1–10^6 Hz; amplitude, 5 mV. The stability of the enzymatic glucose sensor was compared with that of the MIP sensor by characterizing the devices chronoamperometrically at a potential of 0 V with a 1 s sampling interval.

Fabrication and evaluation of the printed wearable sweat sensors

Fabrication and characterization of the microfluidics. The microfluidics layers were fabricated layer-by-layer with a laser cutter by patterning double-sided M-tape and PET with iontophoresis gel reservoirs, a bottom accumulation reservoir, sweat inlets, a sweat collection reservoir and an outlet channel. The detailed fabrication procedures of the microfluidics and the iontophoresis gel are provided in our previous report[22].

Electronic system design and integration of the wearable sweat sensor. A compact and flexible two-layer printed circuit board (FPCB), 13 mm × 46 mm, was engineered. The FPCB's electronic components include a power-managing voltage regulator (ADP162, Analog Devices) and a boost converter (TPS61096, Texas Instruments) for energy efficiency. The FPCB also incorporates a BJT array (BCV62C, Nexperia) and an analogue switch (DG468, Vishay Intertechnology), which play a crucial role in inducing sweat through iontophoresis. At the heart of its functionality is an electrochemical analogue front-end (AFE; AD5941, Analog Devices) coupled with an operational amplifier (LPV811, Texas Instruments), serving as the interface for the sensor array. The system's control and wireless communication capabilities are powered by a Bluetooth low-energy (BLE) module (CYBLE-222014-01, Cypress Semiconductor), which is programmed via PSoC Creator 4.3. This module, through its GPIO pins, triggers the iontophoresis electrodes to stimulate sweat production. Following the stimulation phase, the BLE module takes charge of the AFE, enabling it to perform DPV from three distinct channels to collect sensor data. When the AFE's internal memory is sufficiently filled with sensor data, it prompts the BLE module to collect and send these data for processing and display, either to a custom mobile app or a dedicated BLE dongle (CY5677, Cypress Semiconductor).

Evaluation of the printed sensors for long COVID monitoring in human participants

Subject recruitment. The evaluation of wearable technology for the non-invasive assessment of AA, CK and Trp present in sweat and serum specimens collected from human subjects strictly adheres to established ethical guidelines as delineated in protocols approved by the institutional review board at the California Institute of Technology (Caltech) (number 19-0892). The study cohort comprises individuals between the ages of 18 and 65 years who are in good health and those with long COVID. Long COVID patients were identified following the guidelines provided by Centers for Disease Control and Prevention based on self-reporting of persistent symptoms lasting more than 3 months following acute COVID-19 infection[48]. Participants must still be experiencing one or more symptoms, such as persistent fatigue, shortness of breath, chest pain, cognitive issues ('brain fog'), joint and muscle pain, palpitations, loss of taste or smell, sleep disturbances, fever, gastrointestinal symptoms, or others. These participants were recruited from both the Caltech campus and nearby communities around Los Angeles. All study participants provided written informed consent prior to their involvement in the research.

Sweat and blood sample collection. For sample collection, an iontophoresis session was conducted using the Model 3700 Macroduct Sweat Collection System to induce and collect sweat. Simultaneously, fresh blood samples were obtained using a finger-prick method. Following a standardized clotting procedure, serum was isolated by centrifuging the blood at 2,000 rcf for 15 min, and promptly stored at a temperature of −80 °C for subsequent analysis.

In vitro analysis of sweat and blood samples. In vitro analysis of sweat and blood samples was performed to investigate the correlation of analytes, specifically AA, CK and Trp levels. The quantification of these analytes was carried out with a microplate reader using assay kits from Abcam (catalogue numbers ab65656, ab65340 and ab211098, respectively).

On-body evaluation of the wearable sensors for long COVID monitoring. The healthy and long COVID participants reported to the laboratory after fasting overnight. Fasting helps standardize the physiological state of individuals, reducing variability due to recent food intake or metabolic processes influenced by digestion or hormonal regulation. After 5 min of iontophoresis applied to the participants, the wearable sensor patches performed sweat sampling, recognition and biosensing for 100 min. The sensor system continuously acquired and transmitted AA, CK and Trp sensor data. The system would start a CV cleaning cycle and then the first DPV scan as the initial background without target incubation. The DPV scan was repeated 7 min later as

the postincubation curve. Immediately after the postincubation DPV, another cycle started with a cleaning/regeneration step, followed by an initial background DPV scan. The collected DPV data were wirelessly transmitted to a user device via Bluetooth in real time, where the molecular data were extracted, calibrated and converted to concentration levels.

On-body evaluation of the wearable sensors with meal challenge. For the nutritional monitoring, the participants reported to the laboratory after fasting overnight. The participants were asked to consume a bottle of protein shake and 30 g strawberry or AA or Trp supplement (1 g each). Over the entire study period, the subject's sweat was sampled periodically and analysed by the wearable patch.

Evaluation of the printed sensors for TDM in cancer patients

Cancer patient participant recruitment. Eighteen patients with body weight over 54 kg were enrolled onto this protocol. Written consent was obtained using forms approved by the institutional review board of City of Hope National Medical Center (number 18380). Thirteen patients successfully participated in sample collection or on-site sweat analysis by an on-body sweat sensor. All patients were diagnosed with haematologic diseases including leukaemia or SCD and received one of the medications of interest as part of treatment.

Sweat and blood sample collection. Sweat was collected using a Macroduct Sweat Collection System. Blood samples were taken at different time points within 24 h of the initial drug administration and processed soon after collection. Plasma and sweat samples were stored in −80 °C until analysis. The concentrations of BU, CY and metabolites were measured in the City of Hope Analytical Pharmacology Core using bioanalytical methods adopted from a previous publication[49].

Quantification of CY in human samples. The LC–MS/MS system consisted of a Shimadzu Prominence HPLC system interfaced to an AB SCIEX QTRAP 5500 system. It was calibrated with a standard solution containing 100 ng ml^{-1} CY in 50% acetonitrile with 0.1% formic acid for both compound-dependent and the source-dependent parameters. Multiple reaction monitoring (MRM) data were acquired with the mass transitions and optimized instrument settings listed in Supplementary Table 4.

The separation was achieved using a Kinetex 2.6 µm C18 100 × 2.1 mm column (Phenomenex). The column temperature was maintained at 40 °C and the flow rate was 0.3 ml min^{-1}. Mobile phase A was 0.1% formic acid in H_2O and mobile phase B was 0.1% formic acid in methanol. The following gradient programme was used: 10–25% B (0–0.1 min), 25–65% B (0.1–5.0 min), 65–80% B (5.0–6.0 min), 80–10% B (6.0–6.1 min), 10% B (hold 6.1–8.0 min). The total run time was 8 min. The autoinjector temperature was maintained at 10 °C and the injection volume was 5 µL. Under optimized assay conditions, the retention times for all analytes are shown in Supplementary Table 4.

Stock and working solution preparation. Stock solutions of CY (1 mg ml^{-1}), Keto-CY (1 mg ml^{-1}), DCCY (1 mg ml^{-1}), CEPM (1 mg ml^{-1}), CY-D_4 (1 mg ml^{-1}) and CEPM-D_4 (1 mg ml^{-1}) were prepared in methanol and kept at −20 °C before use. At least two batches of standard stock solution were prepared, one for use as a calibrator and the other as a quality control.

Working calibrator solutions of CY and its metabolites were prepared by serial dilution with methanol. The concentrations for CY were 1,000, 2,000, 10,000, 50,000, 250,000 and 500,000 ng ml^{-1}; the concentrations for Keto-CY, DCCY and CEPM were 100, 200, 1,000, 5,000, 25,000 and 50,000 ng ml^{-1}. Quality-control working solutions of CY and its metabolites were prepared by serial dilution with methanol. The concentrations for CY were 3,000, 30,000 and 450,000 ng ml^{-1}; the concentrations for Keto-CY, DCCY and CEPM were 300, 3,000 and 45,000 ng ml^{-1}. Solutions of CY-D_4 and CEPM-D_4 at 1,000 ng ml^{-1} were prepared in methanol.

Plasma and sweat calibrators and controls. The calibrators and quality controls for CY and its metabolites were prepared individually by mixing 90 µl of pooled plasma or artificial sweat (buffered with pH at 7.0) and 10.0 µl of the calibrator and quality-control working solutions of CY and its metabolites.

Deproteinization of plasma samples. Plasma sample (20 µl) was mixed with 50 µl of a mixed solution of internal standards (1 µg ml^{-1}) and 100 µl methanol, and vortexed for 30 s. A double blank was mixed with 150 µl of methanol. Following centrifugation at 15,000 rcf for 10 min at 4 °C, 50 µl of the supernatant was pipetted into a 1.5 ml microcentrifuge tube and mixed with 200 µl of water, and 5 µl of the sample was then injected.

Preparation of sweat samples. Each 5 µl sweat sample (except the double blank) was mixed with 5 µl of a mixed solution of internal standards and 50 µl 50% methanol, and vortexed for 30 s. A double blank was mixed with 5 µl methanol and 50 µl 50% methanol. Following centrifugation at 15,000 rcf for 15 min at 4 °C, 50 µl of the supernatant was pipetted into a 1.5 ml microcentrifuge tube and 5 µl was injected.

Quantification of busulfan in human plasma, saliva and sweat. LC–MS/MS analysis was performed using a Waters Acquity Class I+ UPLC system interfaced with a Waters Xevo TQ-XS mass spectrometer. HPLC separation was achieved using a LUNA 3 µm C8 20 × 2.0 mm column (Phenomenex). The column temperature was maintained at 30 °C. The mobile phase consisted of 2 mM ammonium formate in water (A) and acetonitrile (B). The following gradient programme was used: 20% B (0–0.8 min, 0.3 ml min^{-1}), 20–90% B (0.8–0.85 min, 0.3 ml min^{-1}), 90% B (0.85–1.3 min, 0.3 ml min^{-1}), 90–20% B (1.3–1.35 min, 0.3 ml min^{-1}), 20% B (1.35–2 min, 0.3 ml min^{-1}). The total run time was 2 min. The autoinjector temperature was maintained at 6 °C. The needle wash solution was water/acetonitrile/methanol (1:1:1, v/v/v), and the wash time was 2 s preinjection and postinjection. The electrospray ionization source of the mass spectrometer was operated in positive-ion mode with a cone gas flow of 150 l h^{-1} and a desolvation gas flow of 1,000 l h^{-1}. The capillary voltage was set to 500 V for both BU and BU-D_8, and the cone and collision cell voltages were optimized to 24 V and 10 eV for both BU and BU-D_8. The source temperature was 150 °C and the desolvation temperature was 500 °C. A solvent delay programme was used from 0 to 0.4 min and from 1.25 to 2 min to minimize the column eluate flowing into the source. MassLynx v.4.2 software was used for data acquisition and processing. Positive electrospray ionization of BU and BU-D_8 produced abundant protonated molecular ions of ammonia adduct $[M + NH_3]^+$. Fragmentation of these compounds was generated by collision-induced dissociation. The precursor → product ion transitions at m/z 264.1 → 151 for BU and 272.1 → 159 for BU-D_8 were used in MRM mode to determine these compounds. The use of MRM provided sufficient specificity and sensitivity. The MS/MS experimental conditions, such as collision energy, were optimized from continuous-flow sample introduction of standard solution.

On-body evaluation of the wearable biosensor for real-time TDM. Two patients diagnosed with AML who received CY as part of their treatment were recruited (the patients received CY infusion at night, one patient had sweat sensed at approximately 13 h after the start of CY infusion, while the other was sensed approximately 15 h after the start of CY infusion). Two patients diagnosed with SCD and AML, respectively, who received BU as part of their treatment were recruited (one was sensed approximately 6 h after BU infusion, while the other was sensed 7 h after the start of BU infusion). After 5 min of iontophoresis applied to the participants, the wearable sensor patches performed

sweat sampling, recognition and biosensing for 100 min. The sensor system continuously acquired and transmitted CY or BU sensor data via Bluetooth. The system would start a CV cleaning cycle and then the first DPV scan as the initial background without target incubation. The DPV scan was repeated 7 min later as the postincubation curve. Immediately after the postincubation DPV, another cycle started with an cleaning/regeneration step, followed by an initial background DPV scan. The collected DPV data were wirelessly transmitted to a user device via Bluetooth in real time, where the molecular data were extracted, calibrated and converted to concentration levels.

Evaluation of the implantable sensor patch in a mouse model

In vivo TDM using the implantable biosensors in mice. The animal studies in this work were performed in accordance with the protocol approved by Caltech Institutional Animal Care and Use Committee (number IA23-1800). In vivo testing was performed using C57BL/6 mice (Jackson Laboratory). Following induction of anaesthesia and analgesia using 2.5% (v/v) isoflurane, Ethiqa XR (3.25 mg kg^{-1}), ketoprofen (5 mg kg^{-1}) and bupivacaine (1 mg kg^{-1}), a 5 mm full-thickness wound was created using a blade and the printed implantable biosensors were implanted into subcutaneous pockets along the dorsomedial skin. Then the incision was sutured using Ethilon 5-0 sterile sutures. After implantation, we tested the sensor in two groups. In one group we injected 10, 20, 30 mg kg^{-1} of CY sequentially. In another group we injected 30 mg kg^{-1} each of the three drugs BU, CY and MPA sequentially. After injection via the tail vein, the sensor signals were recorded every 10 min.

Characterization of the in vivo biocompatibility of the implantable sensor patch. To evaluate the biodegradability and biocompatibility of the implantable patch, we used a murine subcutaneous implantation model with mice obtained from Jackson Laboratory. After anaesthesia and analgesia, a 5 mm full-thickness incision was carefully made using a blade. Subsequently, biosensors were implanted into subcutaneous pockets, along the dorsomedial skin. For biostress evaluation, 200 DPV scans per day were performed on the sensor patch throughout the implantation period. Postimplantation, the incision was meticulously sutured. Animals were humanely killed after 7 and 14 days, and the samples, along with their surrounding tissues, were explanted. The specimens were then preserved in 4% paraformaldehyde at 4 °C overnight, followed by thorough washing with Dulbecco's phosphate-buffered saline repeated five times. Subsequently, the samples underwent an overnight incubation in 30% sucrose at 4 °C. The next step involved embedding the samples in optimal cutting temperature compound (Thermo Fisher Scientific) and rapid freezing using liquid nitrogen. Cryosectioning was then performed, and the resulting sections were stained with haematoxylin and eosin and subjected to immunohistochemistry. For immunohistochemical staining, primary antibodies such as anti-CD3 (SP7) (ab16669) and anti-CD68 (FA-11) (25-0681-82) were utilized, with the secondary antibody being goat anti-rabbit IgG H&L (Alexa Fluor 488) and anti-CD68 antibodies conjugated with PE-Cyanine7 (Invitrogen). To visualize cell nuclei, counterstaining with 4′,6-diamidino-2-phenylindole was performed. Finally, the slides were mounted using ProLong Diamond Antifade Mountant (Invitrogen) and imaged using an LSM 800 confocal laser scanning microscope (Zeiss).

Reporting summary

Further information on research design is available in the Nature Portfolio Reporting Summary linked to this article.

Data availability

The main data supporting the results in this study are available within the paper and its Supplementary Information. Source data are provided with this paper.

References

47. Sun, Q. et al. PySCF: the Python-based simulations of chemistry framework. *WIREs Comput. Mol. Sci.* **8**, e1340 (2018).
48. Chou, R. et al. Long COVID definitions and models of care: a scoping review. *Ann. Intern. Med.* **177**, 929–940 (2024).
49. Rezvani, A. R. et al. Cyclophosphamide followed by Intravenous targeted busulfan for allogeneic hematopoietic cell transplantation: pharmacokinetics and clinical outcomes. *Biol. Blood Marrow Transplant.* **19**, 1033–1039 (2013).

Acknowledgements

This project was supported by National Science Foundation grant 2145802, National Institutes of Health grants R01HL155815, R21DK13266, U01CA239373 and R01GM129863, American Cancer Society Research Scholar Grant RSG-21-181-01-CTPS, Office of Naval Research grants N00014-21-1-2483 and N00014-21-1-2845, Army Research Office grant W911NF-23-1-0041, NASA Cooperative Agreement 80NSSC20M0167, Heritage Medical Research Institute, and Caltech-City of Hope Biomedical Initiative Pilot Grant. We gratefully acknowledge critical support and infrastructure provided for this work by the Kavli Nanoscience Institute at Caltech. Research reported in this publication includes work performed in the Analytical Pharmacology Core supported by the National Cancer Institute of the National Institutes of Health under grant P30CA033572. The content is solely the responsibility of the authors and does not necessarily represent the official views of the National Institutes of Health.

Author contributions

W.G. and M.W. initiated the concept and designed the studies. M.W., C.Y., Y.Y., D.M., C.W., C.X., S.A.S., J.T. and S.T. performed sensor characterization, validation and sample analysis. J.M. contributed to the signal processing and app development. T.K.H., Z.L., G.S. and J.S.M contributed to the sensor evaluation in human subjects. W.G. and M.W. co-wrote the paper. All authors contributed to the data analysis and provided the feedback on the paper.

Competing interests

The authors declare no competing interests.

Additional information

Supplementary information The online version contains supplementary material available at https://doi.org/10.1038/s41563-024-02096-4.

Correspondence and requests for materials should be addressed to Wei Gao.

Peer review information *Nature Materials* thanks Nicolas Voelcker and the other, anonymous, reviewer(s) for their contribution to the peer review of this work.

nature research

Corresponding author(s): Wei Gao

Last updated by author(s): Nov 4, 2024

Reporting Summary

Nature Research wishes to improve the reproducibility of the work that we publish. This form provides structure for consistency and transparency in reporting. For further information on Nature Research policies, see our Editorial Policies and the Editorial Policy Checklist.

Statistics

For all statistical analyses, confirm that the following items are present in the figure legend, table legend, main text, or Methods section.

n/a	Confirmed	
☐	☒	The exact sample size (*n*) for each experimental group/condition, given as a discrete number and unit of measurement
☐	☒	A statement on whether measurements were taken from distinct samples or whether the same sample was measured repeatedly
☒	☐	The statistical test(s) used AND whether they are one- or two-sided *Only common tests should be described solely by name; describe more complex techniques in the Methods section.*
☒	☐	A description of all covariates tested
☒	☐	A description of any assumptions or corrections, such as tests of normality and adjustment for multiple comparisons
☐	☒	A full description of the statistical parameters including central tendency (e.g. means) or other basic estimates (e.g. regression coefficient) AND variation (e.g. standard deviation) or associated estimates of uncertainty (e.g. confidence intervals)
☒	☐	For null hypothesis testing, the test statistic (e.g. *F*, *t*, *r*) with confidence intervals, effect sizes, degrees of freedom and *P* value noted *Give P values as exact values whenever suitable.*
☒	☐	For Bayesian analysis, information on the choice of priors and Markov chain Monte Carlo settings
☒	☐	For hierarchical and complex designs, identification of the appropriate level for tests and full reporting of outcomes
☐	☒	Estimates of effect sizes (e.g. Cohen's *d*, Pearson's *r*), indicating how they were calculated

Our web collection on statistics for biologists contains articles on many of the points above.

Software and code

Policy information about availability of computer code

Data collection	Mbed was used to program microcontroller. CH Instrument 840D and 760 were used for off-body sensor data collection.
Data analysis	Microsoft Excel 2021 and Origin 2021 were used to analyze all data, plot the data and calculate the statistical parameters.

For manuscripts utilizing custom algorithms or software that are central to the research but not yet described in published literature, software must be made available to editors and reviewers. We strongly encourage code deposition in a community repository (e.g. GitHub). See the Nature Research guidelines for submitting code & software for further information.

Data

Policy information about availability of data

All manuscripts must include a data availability statement. This statement should provide the following information, where applicable:

- Accession codes, unique identifiers, or web links for publicly available datasets
- A list of figures that have associated raw data
- A description of any restrictions on data availability

The data that support the plots within this paper are available from the corresponding author upon request.

Field-specific reporting

Please select the one below that is the best fit for your research. If you are not sure, read the appropriate sections before making your selection.

☒ Life sciences ☐ Behavioural & social sciences ☐ Ecological, evolutionary & environmental sciences

For a reference copy of the document with all sections, see nature.com/documents/nr-reporting-summary-flat.pdf

Life sciences study design

All studies must disclose on these points even when the disclosure is negative.

Sample size	For on body evaluation of the wearable sensor, 12 healthy subjects were recruited, for the Long COVID study, 3 Long COVID subjects were recruited, and 3 healthy subjects were involved; for the supplement intake study, 3 healthy subjects were involved for each study; for the on-body evaluation of the wearable drug sensors, 4 cancer patients (2 with sickle cell disease (SCD) who received CY, and 2 patients diagnosed with acute myeloid leukemia (AML) and SCD who received treatment with BU). Sample sizes were chosen on the basis of standards in the literature for proof-of-concept experiments.
Data exclusions	No data exclusion.
Replication	Results were replicated in independent experiments as described in the manuscript. Every experiment included replicates as described in the figure legends and experimental methods.
Randomization	The device was fabricated with same process and was tested in all participants under same conditions. Randomization was therefore not relevant to the study.
Blinding	Not relevant, because a blinding process wouldn't influence the sampling result.

Reporting for specific materials, systems and methods

We require information from authors about some types of materials, experimental systems and methods used in many studies. Here, indicate whether each material, system or method listed is relevant to your study. If you are not sure if a list item applies to your research, read the appropriate section before selecting a response.

Materials & experimental systems

n/a	Involved in the study
☐	☒ Antibodies
☐	☒ Eukaryotic cell lines
☒	☐ Palaeontology and archaeology
☐	☒ Animals and other organisms
☐	☒ Human research participants
☒	☐ Clinical data
☒	☐ Dual use research of concern

Methods

n/a	Involved in the study
☒	☐ ChIP-seq
☒	☐ Flow cytometry
☒	☐ MRI-based neuroimaging

Antibodies

Antibodies used	anti-CD3 [SP7] (ab16669) and anti-CD68 (ab31630) from Abcam.
Validation	N/A

Eukaryotic cell lines

Policy information about cell lines

Cell line source(s)	Normal Adult human dermal fibroblast cells (HDFs, Lonza).
Authentication	All cells were purchased from Lonza and have been ethically sourced and authenticated by thorough QC testing by Lonza.
Mycoplasma contamination	We did not observe any mycoplasma contamination in our cell cultures.
Commonly misidentified lines (See ICLAC register)	N/A

Animals and other organisms

Policy information about studies involving animals; ARRIVE guidelines recommended for reporting animal research

Laboratory animals	C57BL/6 mice (The Jackson Laboratory, Bar Harbor, ME, USA)
Wild animals	No wild animals were used in the study.
Field-collected samples	No field collected samples were used in the study.
Ethics oversight	The animal protocol was approved by the Institutional Animal Care and Use Committee (IACUC) (Protocol No. IA23-1800) at California Institute of Technology.

Note that full information on the approval of the study protocol must also be provided in the manuscript.

Human research participants

Policy information about studies involving human research participants

Population characteristics	For Long COVID study, the study cohort comprises individuals between the ages of 18 and 65 who are in good health and Long COVID (signs, symptoms, and conditions that continue or develop after acute COVID-19 infection) with a body mass index (BMI) of 18.5 to 24.9 kg m-2. For therapeutic drug monitoring, eighteen patients with body weight over 14 kilograms regardless of gender were enrolled onto this protocol.
Recruitment	The healthy and Long COVID participating subjects were recruited from Caltech campus, the neighboring communities through advertisement by posted notices, word of mouth, and email distribution. The cancer patients were recruited from City of Hope. There were no self-selection biases or other biases. All participants gave written informed consent before participation in the study.
Ethics oversight	Institutional Review Board (IRB) at the California Institute of Technology; National Medical Center of City of Hope

Note that full information on the approval of the study protocol must also be provided in the manuscript.